Fabrication of a TiO$_2$/Fe$_2$O$_3$ Core/Shell Nanostructure by Pulse Laser Deposition toward Stable and Visible Light Photoelectrochemical Water Splitting

Hao Lu,* Song Fang, Jundie Hu, Bo Chen, Run Zhao, Huishu Li, Chang Ming Li,* and Jinhua Ye

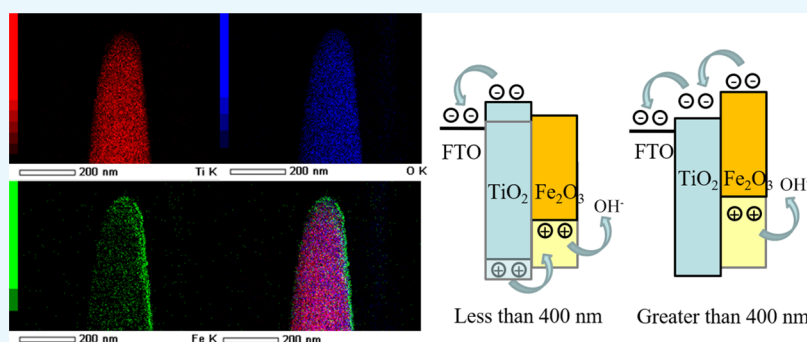Cite This: *ACS Omega* 2020, 5, 19861−19867

Read Online

ACCESS | Metrics & More | Article Recommendations | SI Supporting Information

ABSTRACT: Here, we report the fabrication of TiO$_2$/Fe$_2$O$_3$ core/shell heterojunction nanorod arrays by a pulsed laser deposition (PLD) process and their further use as photoelectrodes toward high-performance visible light photoelectrochemical (PEC) water splitting. The morphology, phase, and carrier conduction mechanism of plain TiO$_2$ and TiO$_2$/Fe$_2$O$_3$ core/shell nanostructure were systematically investigated. PEC measurements show that the TiO$_2$/Fe$_2$O$_3$ core/shell nanostructure enhances photocurrent density by nearly 2 times than the plain ones, increases visible light absorption from 400 to 550 nm, raises the on/off separation rate, and delivers high stability with only a 3% decrease of current density for tests of even more than 14 days. This work provides a method to design an efficient nanostructure by combination of a facile hydrothermal process and high-quality PLD process to fabricate a clean surface and excellent crystallinity for charge separation, transfer, and collection toward enhanced PEC properties.

1. INTRODUCTION

Photoelectrochemical (PEC) water splitting is one of the promising methods to directly convert solar energy to chemical energy by using semiconductor electrodes.[1−4] Since the discovery of Fujishima and Honda in 1972, various photomaterials have been fabricated for PEC water splitting systems toward high stability and efficiency.[5] Compared with other well-known wide gap metal oxides like ZnO, SnO$_2$, and SrTiO$_3$, TiO$_2$ exhibits several prominent properties such as chemical stability, high charge mobility, and low cost.[6−9] Li et al. reported a new TiO$_2$ structure with a nanofiber template to have a quite high current density.[10] Liu et al. made a black TiO$_2$ with the use of Ar and Ar/H$_2$ gas to achieve more light absorbance for a higher hydrogen production rate.[11] Wu et al. demonstrated a Bi-TiO$_2$ nanostructure to deliver high performance.[12] Obviously, it is still very challenging to accomplish an excellent efficiency by TiO$_2$ alone as its light absorption ability is limited by the wide band gap only for UV light, which is a small part of the full spectrum. In consideration of expanding light absorption ability, hematite (α-Fe$_2$O$_3$) is one of the most promising candidate materials due to its narrow band gap ($\sim$2.0 eV), good response to visible light, environmental friendliness, earth abundance, and the con-

duction band edge position for possible water splitting at a low voltage.[13−16] Yu et al. prepared a quite high-performance hematite photoanode by the pulsed laser deposition (PLD) approach and further used more FeOOH loading on the hematite layer to have nearly 0.8 mA cm^{-2} at 1.23 V versus reversible hydrogen electrode (RHE).[17] Wang et al. demonstrated a Sn-doped hematite nanoflake to increase the photocurrent.[18] Han et al. reported a Sb-doped SnO$_2$ (ATO) with Fe$_2$O$_3$ nanorods for water splitting, and the efficiency of the best sample has increased 139% higher than that of the pure hematite nanorods at 1.23 V$_{RHE}$.[19] However, it is noticed that their devices demand complicated experiment processes and additional added materials, which would restrict inevitably the practical applications in the future.
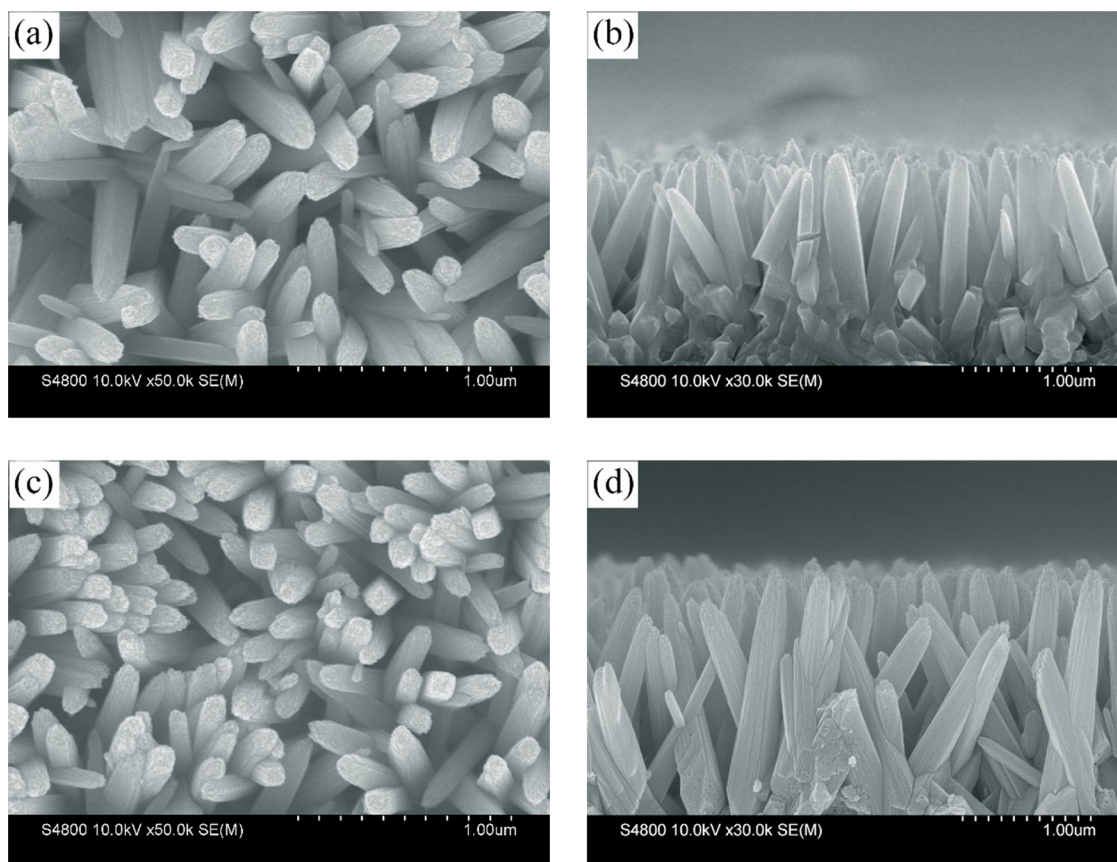
Figure 1. SEM images of the (a) top view and (b) cross section of TiO_2. (c) Top view and (d) cross section of the TiO_2/7 min Fe_2O_3 core/shell nanostructure.

Even up to now, it is still difficult to succeed a high-performance electrode by only one material due to the great restriction of the individual's own flaws. Photogenerated charges require efficient separation followed by fast transportation to inject into the respective reduction and oxidation reactions, but the charges are very tough to be generated and separated in one material alone. We argue that we could expect to build a core/shell nanostructure, in which a high charge mobility material as a core improves the transmission efficiency of photoinduced charges and a wide light spectrum absorption material as a shell enhances the visible light response and charges separation.[20−22] Yang et al. prepared a TiO_2/$BaTiO_3$ core/shell nanostructure, which produced a high photocurrent, but both materials could absorb only UV light.[23] Wang et al. devised Fe_2O_3/TiO_2 core/shell photoelectrodes to improve separate efficiency of photo-induced charge carriers and absorb visible light.[24] Smith et al. reported TiO_2/WO_3 and WO_3/TiO_2 core/shell nanorod arrays to combine optical utilization and water splitting efficiency together.[25] Though these works used various types of materials, they chose the same facile way to prepare the nanostructure by using arrays as a core and high-quality materials as a shell. PLD is a powerful tool for depositing thin films with great precision in thickness and quality at a controllable laser intensity and frequency.[26−29] The high-quality target and feathering deposition process of PLD endorse the perfect ability to produce conformal ultrahigh-quality films under a low temperature.

Here, we employ a PLD technique to deposit Fe_2O_3 films with different thicknesses on TiO_2 nanorod arrays at a temperature of 500 °C, which is much lower than the traditional crystallization temperature (700 °C). After an annealing process, the as-prepared high-quality TiO_2/Fe_2O_3 core/shell nanostructures are firmly attached on the F-doped tin oxide (FTO) substrate and are further used for the photoanode in the water splitting system. The thickness of the Fe_2O_3 film can be tuned precisely for effective light utilization and photogenerated charge transport by controlling the deposition times. The TiO_2/Fe_2O_3 core/shell photoanode shows a high current density of 0.91 mA cm^{-2} at 1.23 V$_{RHE}$, which is 165% higher than that of the plain TiO_2 nanorod array photoanode (0.55 mA cm^{-2}). It is worthy to note that the spectral absorption is extended to nearly 600 nm while the photocurrent still remains more than 97% after about 14 days of continuous testing. The mechanism for the photoelectric properties increasing is studied by investigating the parameters, including the morphological changes, the thickness of the PLD Fe_2O_3 layer, transmittance rate, crystal structure, and electrochemical impedance spectroscopy (EIS). The TiO_2/Fe_2O_3 core/shell photoanode is further studied from the band gap view toward increasing the photogenerated conduction band to reveal the fundamental insights behind.

2. RESULTS AND DISCUSSION

Figure 1 shows the SEM image of the morphology of TiO_2 nanorod arrays and the sample after Fe_2O_3 loading. Figure 1a shows uniform and typical TiO_2 nanorod arrays with about 150 nm diameter and a smooth top-side. From Figure 1b, we can see that the length of TiO_2 nanorods is about 1.8 μm, which has been viewed as the suitable thickness for charge transport.[24,30] Also, different lengths of TiO_2 have been prepared, which could be found in Figure S1, and the 1.8 μm sample shows the best performance. Figure 1c,d gives the representative top-view and

cross-sectional SEM images of TiO_2/7 min Fe_2O_3 core/shell nanostructures, which were measured as the best samples in the following discussion. During the PLD process, high energy laser pulses bombard the surface of the Fe_2O_3 target and deposit it onto TiO_2. From the top-view SEM image of Figure 1c, there is only little roughness change on the surface and all nanorods have similar morphologies. From the cross-sectional image of Figure 1d, we can identify that the top-side and down-side have nearly the same surface. We also prepared a 30 min long deposited time sample from which we can see that the morphology has been totally changed with a large amount of Fe_2O_3 (Figure S2). Through the comparison before and after the deposition of Fe_2O_3, we can see that a uniform film is well prepared by using PLD technology.

To discuss the crystallization state and the uniformity of the nanostructure after PLD Fe_2O_3 deposition, the XRD pattern (Figure 2a) was used here.
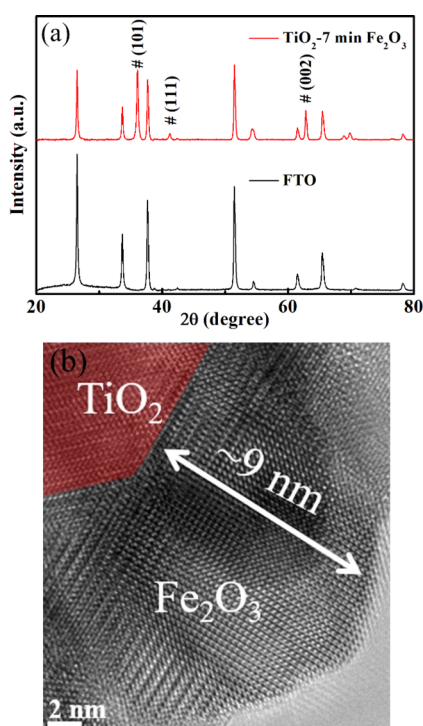

Figure 2. (a) XRD patterns of FTO glass and TiO_2/7 min Fe_2O_3 core/shell nanostructure. (b) HRTEM of the TiO_2/7 min Fe_2O_3 core/shell nanostructure.

However, the characteristic peaks of Fe_2O_3 are hard to detect owing to the short depositing time, but the peaks of TiO_2 can be detected easily due to its excellent crystallinity, which can be indexed to the rutile type (JCPDS no. 88-1175).[31] To further identify Fe_2O_3, we deposited Fe_2O_3 on Si under the same experimental condition, and the XRD pattern could be found in Figure S3 from which we can see the peak of Fe_2O_3. From the HRTEM image (Figure 2b), we can see more details about the sample of the TiO_2/7 min Fe_2O_3 nanostructure. The image shows that the Fe_2O_3 thin film has a high-quality crystalline structure with a clean external surface and ~9 nm thickness, which is good for charge transport. The selected area electron diffraction (SAED) pattern (Figure S4) of TiO_2/7 min Fe_2O_3 shows that it has very high crystallinity. A larger scale of Fe_2O_3 could be found in Figure S5 from which the surface of Fe_2O_3 is still clear. The TEM and SAED images of the TiO_2 sample in

Figure S6 show that the TiO_2 nanorod has the (110) plane. In addition, it would be pertinent to mention that the surface (110) of the rutile has been shown to be highly active for photocatalytic water splitting as well as for applications in the areas of catalysis and photochemistry.[32,33] The surface of TiO_2 is like most hydrothermal crystals but not as clean as Fe_2O_3, which has a sharp surface. It is easy to identify the different elements from the EDAX mapping (Figure 3) of a single nanorod in which the green color shows that Fe of the Fe_2O_3 layer is continuously deposited on the surface of TiO_2 not just on the top.
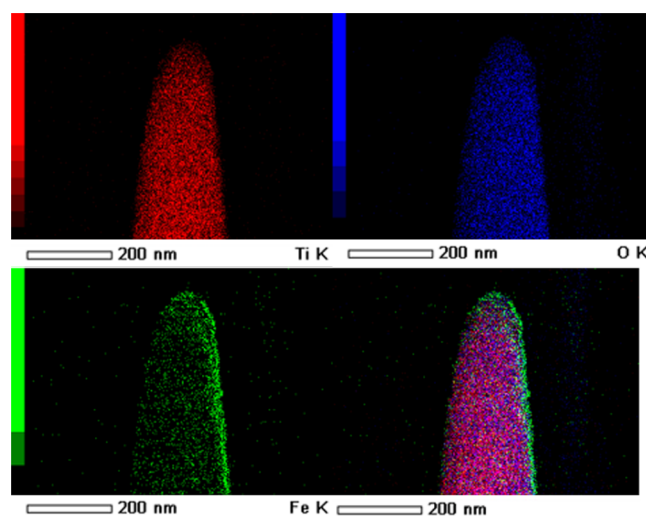

Figure 3. EDAX mapping of the TiO_2/7 min Fe_2O_3 core/shell nanostructure by TEM.

Due to this, TEM only has one detector from one side to collect signals; the right side is brighter than the left side. The EDAX mapping from SEM (Figure S7) used here to identify large-sized nanorod arrays also showed the Fe being uniformly deposited from the top to the down-side of TiO_2 nanorod arrays in which the red color shows Fe and the blue color shows Ti. Also, from the EDAX mapping of SEM, the atomic amount of Fe is only 3.9% (Table S1). Both morphology and elemental analysis show that an excellent Fe_2O_3 layer with a clean surface and high-quality crystalline structure can be obtained by this PLD process, which is good for the building of the TiO_2/Fe_2O_3 core/shell nanostructure.

The electrochemical and optical performances for the varieties of TiO_2/Fe_2O_3 photoanodes with changing deposition times and TiO_2 photoanode are shown in Figure 5. Absorbance curves of different Fe_2O_3 deposited time samples in Figure 4a indicate that increasing the deposition time can increase the
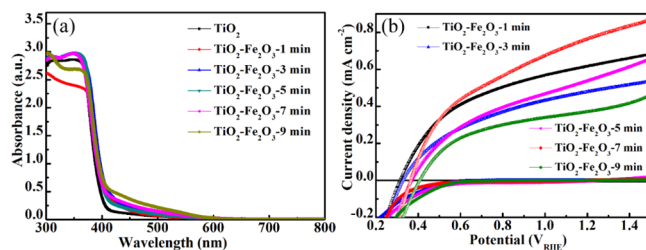

Figure 4. (a) Absorbance spectra of TiO_2 and different deposited time TiO_2/Fe_2O_3 core/shell nanostructures. (b) $J-V$ curves of different Fe_2O_3 deposited core/shell nanostructures.
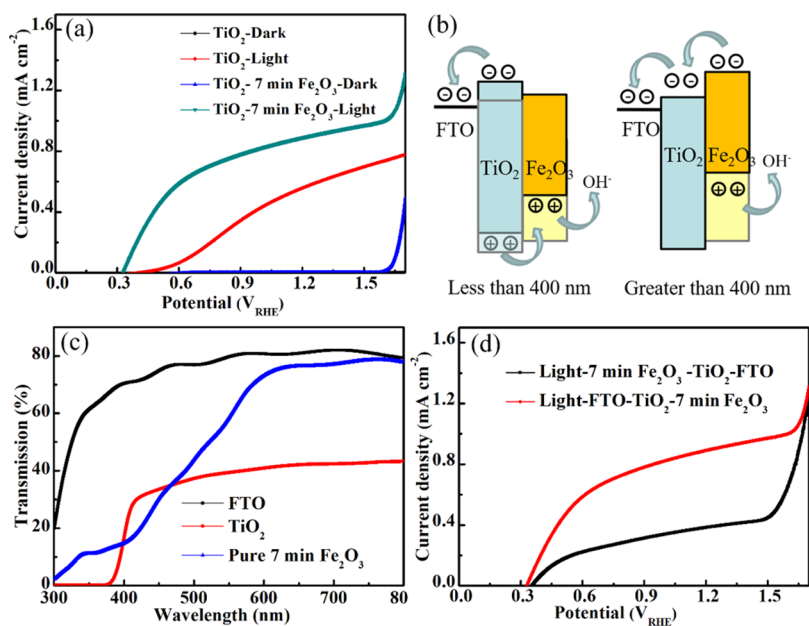
Figure 5. (a) $J-V$ curves of TiO_2 and the $TiO_2/7$ min Fe_2O_3 core/shell nanostructure. (b) Band gap matching of the $TiO_2/7$ min Fe_2O_3 core/shell nanostructure with different light wavelengths. (c) Transmission spectra of different substrates. (d) $J-V$ curves of the $TiO_2/7$ min Fe_2O_3 core/shell nanostructure with different illumination sides.

absorption edge to absorb more visible light. The thickness of the Fe_2O_3 layer is the most important part in this nanostructure in which the thicker Fe_2O_3 layer can absorb more light, but the thinner Fe_2O_3 layer has better electrotransport performance.

Figure 4b shows the $J-V$ curves of different Fe_2O_3 deposited times under AM 1.5G irradiation (100 mW cm^{-2}). The current density increased with increasing deposition time from 1 to 7 min and then decreased at 9 min in which the very thick Fe_2O_3 layer can destroy the charge transport ability of the core/shell nanostructure due to the poor charge transport of Fe_2O_3. According to the Nernst equation

$$E_{RHE} = E_{Ag/AgCl} + 0.059pH + E^o{}_{Ag/AgCl}$$

where E_{RHE} is the converted potential versus RHE and $E^o{}_{Ag/AgCl}$ = 0.1976 V at 25 °C; the potential that is tested by the Ag/AgCl and 1 M KOH (pH ~13.6) system can be converted to the RHE system. The current density of the $TiO_2/7$ min Fe_2O_3 device is 0.91 mA cm^{-2}, and the TiO_2 device is nearly 0.55 mA cm^{-2} in Figure 5a at 1.23 V versus RHE. Also, Figure 5a displays a reduced onset potential, which indicates the enhanced PEC water oxidation kinetics. The M-S measurement used here and shown in Figure S8, which displays a reduced onset potential of the TiO_2/Fe_2O_3 sample, indicates the enhanced PEC water oxidation kinetics. Generally, the conduction band (CB) of TiO_2 is (−4.1 eV) higher than that of Fe_2O_3 (−4.7 eV) and the valence band (VB) of TiO_2 is (−7.2 eV) lower than that of Fe_2O_3 (−7.0 eV) in the vacuum system.[34,35] Considering the band gap of these two materials, this core/shell nanostructure may not be suitable for carrier separation and transport to react with hydroxyl. In consideration, we propose a new carrier transport theory combined with photopotential with different light wavelengths; the translucent one represents the original band gap position, and the darker one represents the band gap after photogeneration (Figure 5b).

We prepared this water splitting system with the order of light source/FTO/TiO$_2$/Fe$_2$O$_3$ (Figure S9) and divided the light wavelength into two parts; one is lower than 400 nm, which

matches the TiO_2 band gap absorption, and one is higher for Fe_2O_3. If the light whose wavelength is lower than 400 nm came from the FTO side to TiO_2 nanorod arrays, both TiO_2 and Fe_2O_3 have photogenerated potential, and almost all light can be absorbed by the TiO_2 nanorod, which can be seen from the transmission spectrum (Figure 5c). Fe_2O_3 can still absorb a small amount of transmitted light to generate photogenerated carriers, but the small amount of photogenerated carriers in this part is difficult to transmit to the external circuit through energy band transition of TiO_2. Therefore, we think that Fe_2O_3 only reflects the conductivity of semiconductor materials in this wavelength's water splitting process and holes can transport to Fe_2O_3 to react with hydroxyl to generate O_2. This process needs a very high quality of Fe_2O_3 films, which could transport most parts of carriers without recombination, and the thickness is also limited by the average diffusion length. If the light whose wavelength is higher than 400 nm came from FTO to the TiO_2/Fe_2O_3 core/shell structure, TiO_2 cannot absorb this part of the light, and Fe_2O_3 can absorb it. Photogenerated voltage will increase the energy band of Fe_2O_3 that is high enough to transport the photocarrier in the water splitting process, and the holes in Fe_2O_3 itself also can react with hydroxyl to get O_2. According to this inference, the thicker Fe_2O_3 layer needs a higher photogenerated voltage to transport the carrier, which is the same as the results of Figure 4b; the thicker Fe_2O_3 sample has a higher onset potential. From the curves of the transmission pattern (Figure 5c), we prepared the sample with FTO glass, a TiO_2 film, and 7 min of Fe_2O_3 directly deposited on FTO glass to check the light absorption capacity of the material itself. We can see that the cross point of two curves is 398 nm, which after that point, light can pass through the TiO_2 to Fe_2O_3. When using light/FTO/TiO$_2$/Fe$_2$O$_3$, almost all light whose wavelength is lower than 400 nm can be absorbed by TiO_2, only the 2 nm part could not be absorbed, and the other part of the light can be absorbed by Fe_2O_3 to get high power conversion efficiency (PCE). However, when we use the light/Fe$_2$O$_3$/TiO$_2$/FTO model, only the 2 nm part of the light can easily pass Fe_2O_3 to be
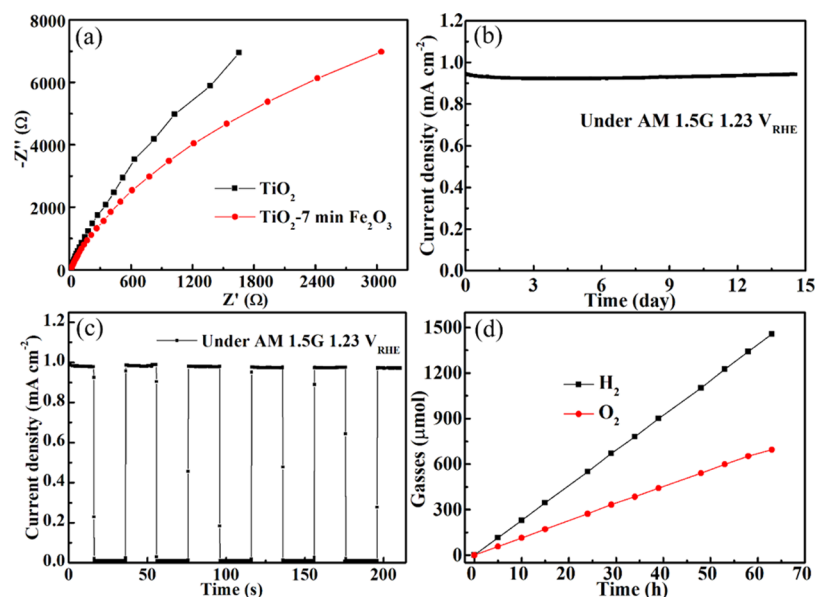
Figure 6. (a) Nyquist plots of TiO_2 and the TiO_2/7 min Fe_2O_3 core/shell nanostructure. (b) Long-time measurement, (c) on/off measurement, and (d) gasses measurement of the TiO_2/7 min Fe_2O_3 core/shell nanostructure under AM 1.5G 1.23 V_{RHE}.

absorbed by TiO_2 and the other matched TiO_2 band gap light may need to be absorbed by Fe_2O_3. Photogenerated carriers need to cross a high energy barrier to transport, which will get a lower PCE. To confirm this conclusion, we prepared the flipped system with the samples tested under the light source/Fe_2O_3/TiO_2/FTO order and the transmittance was measured. As seen in Figure 5d, the value of the light/Fe_2O_3/TiO_2/FTO sample at 1.23 V on the black curve is about 0.45 mA cm^{-2} lower than that of the light/FTO/TiO_2/Fe_2O_3 sample and the value of the light/Fe_2O_3/TiO_2/FTO sample is even lower than that of the TiO_2 one. To further confirm this, a filter was used here to remove the wavelength that was higher than 400 nm and was put between the light source and TiO_2/7 min Fe_2O_3 sample; the J–V curves are shown in Figure S10. When we measured like the order in Figure S8, the current density of the filter-used sample is similar to that of the TiO_2 sample. However, when we illuminated from the back side with the light/Fe_2O_3/TiO_2/FTO order, the current density has a significant reduction.

To gain deeper insight into the charge transfer and recombination processes before and after Fe_2O_3 treatment, the EIS measurement was used here. During this measurement, both TiO_2 and TiO_2/7 min Fe_2O_3 core/shell samples were tested under AM 1.5G (Figure 6a). When samples were measured under the light model, the smaller radius of Nyquist plots meant a less recombination rate. We can see that the radius of the TiO_2/7 min Fe_2O_3 curve is smaller than that of the TiO_2 one, meaning that TiO_2/7 min Fe_2O_3 has a less recombination rate than TiO_2. We attribute this result to the clean surface and high-quality crystalline structure of a PLD-prepared Fe_2O_3 thin film, which directly contacts with the electrolyte. The Nyquist plots of Fe_2O_3 with different deposited times were measured and are shown in Figure S11 in which the 7 min sample also shows the best performance.

The stability measurement was executed over the TiO_2/7 min Fe_2O_3 core/shell sample for more than 1 week. From Figure 6b, we can see that the current density still remains high after 14 days of measurement and exhibits only a 3% decrease. The performance of devices even has increased after 84 h, which can be considered as temperature increased by continuous exposure.

The pristine TiO_2 prepared water splitting cells were also tested for 30,000 s and are shown in Figure S12, which has obviously decreased with long-time measurement. We consider that this low decay can be attributed to a high quality of a PLD-prepared Fe_2O_3 film and effective charge transport in this core/shell nanostructure. From the on/off light measurement also prepared in Figure 6c, we can see that there are nearly no peaks at the light on and light off point. This measurement also shows that the sample has good charge separation capability. The gas evolution measurement was also used here to check the products, and all electrodes are sealed in a container and connected to the gas detection device (Figure S13) and tested under AM 1.5G with 1.23 V_{RHE}. From Figure 6d, the rate for O_2 evolution is about 10.7 μmol h^{-1} cm^{-2} and there is no obvious decay after 70 h of testing. O_2 evolution is nearly the same with half the amount of holes passing through the outer circuit, which means that almost all the holes were used for water oxidation. From these analyses, the TiO_2/Fe_2O_3 core/shell nanostructure provides several advantages of effective light absorption, photogenerated carrier separation, and low recombination rate, thus resulting in improved PEC performance.

3. CONCLUSIONS

In summary, we designed and investigated TiO_2/Fe_2O_3 core/shell nanostructures as photoanodes for PEC water splitting. Due to the high-quality PLD-prepared Fe_2O_3 shell, the photocurrent density is enhanced to 0.91 mA cm^{-2} under AM 1.5G, which is nearly twice as high as that of plain TiO_2. The effective visible light absorption, excellent carrier transport and separation, and low recombination rate synergistically contribute to the enhanced PEC water splitting performance. We hope that our findings open a promising route to design complex nanostructures by using unconventional technologies and can be universally applied in other solar energy fields.

4. EXPERIMENTAL SECTION

4.1. Preparation of Photoanodes. These photoanodes were fabricated on FTO substrates, which were washed for 30 min each with acetone, ethyl alcohol, and deionized water in an

ultrasonic bath. First, the TiO_2 nanorod arrays were prepared by a chemical hydrothermal method. Precursor solution consisted of 0.269 g of citric acid (anhydrous; Sigma-Aldrich), 1 mL of titanium(IV) butoxide (97%; Sigma-Aldrich), 30 mL of hydrochloric acid (36.5−38%; Sigma-Aldrich), and 30 mL of deionized water. A cleaned FTO substrate was immersed in the precursor of a 100 mL Teflon-lined stainless steel autoclave with the conductive side facing downward. The autoclave was put into the oven before opening the heating procedure. The autoclave was heated to 155 °C for 6 h and naturally cooled to room temperature. After the reaction process, the samples were rinsed with deionized water to remove the foreign matters deposited on the surface of the sample. Second, TiO_2/Fe_2O_3 photoanodes were prepared by the PLD (STPLD; Pascal Co. Ltd., Japan) method using Fe_2O_3 pellets (Hefei Kejing Co. Ltd., China) as targets and the prepared TiO_2 nanostructure as a substrate. The temperature for deposition was 550 °C. The chamber of the PLD machine was first evacuated lower than 10^{-4} Pa. For the preparation of Fe_2O_3, pure O_2 was introduced into the chamber until the pressure became 3−4 Pa. The laser was used to irradiate for different amounts of time, and we took a sample every 2 min, namely, 1, 3, 5, 7, and 9 min. After the laser irradiation, the film was kept at 550 °C for 30 min as a post-heat treatment.

4.2. Characterization. The morphology of the samples was characterized using field-emission scanning electron microscopy (FE-SEM; Hitachi, S4800) and high-resolution transmission electron microscopy (HRTEM; Jeol, JEM2100F). The phase of products was checked by X-ray diffraction (XRD, RIGAKU Rint-2000 X-ray diffractometer, Cu Kα radiation, λ = 0.15418 nm). The current density versus potential and incident photon-to-current conversion efficiency (IPCE) were measured using a WXS-80C-3 solar simulator under AM 1.5G (100 mW cm^{-2}). The absorbance and transmission spectra were detected using a UV−vis spectrophotometer (Shimadzu UV-2500). Electrochemical impedance spectroscopy (EIS) and Mott−Schottky (M-S) were measured with an electrochemical workstation (ALS/CH model 650A) under light with an alternative signal amplitude of 5 mV and a frequency range of 1.0×10^5 to 4.0×10^5 Hz.

4.3. Photoelectrochemical Measurements. Photoelectrochemical measurements were carried out in the electrolyte containing 1 M KOH (pH ∼13.6) under a three-electrode system. The work electrodes were the as-prepared FTO/TiO_2 or FTO/TiO_2/Fe_2O_3 samples, the counter electrode was a Pt sheet, and the reference electrode was a saturated Ag/AgCl electrode. Before the measurement, the inert gas Ar was used to remove the dissolved oxygen in the electrolyte for about 30 min and it was kept under the process of testing. The long-time stability and time curves with light on/off cycle measurements were performed in a closed system under simulated AM 1.5G solar illumination. The curves were recorded by scanning the potential from the negative to the positive direction with a scan rate of 0.01 V s^{-1}. M-S plots were obtained by the same workstation at an AC frequency of 10^3 Hz with an amplitude of 5 mV under light.

ASSOCIATED CONTENT

⑤ Supporting Information

The Supporting Information is available free of charge at https://pubs.acs.org/doi/10.1021/acsomega.0c02838.

Morphology characterization: SEM and TEM images; elemental analysis: SAED, EDAX, and XRD pattern; electrochemical testing: J−V measurement, J−t measurement, and Nyquist measurement; and schematic and photo of devices (PDF)

AUTHOR INFORMATION

Corresponding Authors

Hao Lu − *Institute of Materials Science & Devices, Suzhou University of Science and Technology, Suzhou 215009, China*; Email: luhaoshaobo@163.com

Chang Ming Li − *Institute of Materials Science & Devices and Jiangsu Key Laboratory of Micro and Nano Heat Fluid Flow Technology and Energy Application, School of Environmental Science and Engineering, Suzhou University of Science and Technology, Suzhou 215009, China; Institute of Advanced Cross-field Science and College of Life Science, Qingdao University, Qingdao 200671, P. R. China; Institute for Clean Energy & Advanced Materials, Southwest University, Chongqing 400715, P. R. China;* ⑩ orcid.org/0000-0002-4041-2574; Email: ecmli@swu.edu.cn

Authors

Song Fang − *Institute of Materials Science & Devices, Suzhou University of Science and Technology, Suzhou 215009, China*

Jundie Hu − *Institute of Materials Science & Devices, Suzhou University of Science and Technology, Suzhou 215009, China*

Bo Chen − *Institute of Materials Science & Devices, Suzhou University of Science and Technology, Suzhou 215009, China*

Run Zhao − *Institute of Materials Science & Devices, Suzhou University of Science and Technology, Suzhou 215009, China*

Huishu Li − *Center for Soft Condensed Matter Physics & Interdisciplinary Research, College of Physics, Optoelectronics and Energy, Soochow University, Suzhou 215006, China*

Jinhua Ye − *International Center for Materials Nanoarchitectonics (WPI-MANA), National Institute for Materials Science (NIMS), Ibaraki 305-0044, Japan;* ⑩ orcid.org/0000-0002-8105-8903

Complete contact information is available at:
https://pubs.acs.org/10.1021/acsomega.0c02838

Notes

The authors declare no competing financial interest.

ACKNOWLEDGMENTS

REFERENCES

(1) Walter, M. G.; Warren, E. L.; McKone, J. R.; Boettcher, S. W.; Mi, Q.; Santori, E. A.; Lewis, N. S. Solar Water Splitting Cells. *Chem. Rev.* **2010**, *110*, 6446−6473.

(2) Liao, A.; Chen, R.; Fan, F.; Xiao, L.; He, H.; Zhang, C.; Asiri, A. M.; Zhou, Y.; Li, C.; Zou, Z. Integration of Fe_xS Electrocatalysts and Simultaneously Generated Interfacial Oxygen Vacancies to Synergistically Boost Photoelectrochemical Water Splitting of Fe_2O_3 Photoanodes. *Chem. Commun.* **2018**, *54*, 13817−13820.

(3) Luo, H.; Zeng, Z.; Zeng, G.; Zhang, C.; Xiao, R.; Huang, D.; Lai, C.; Cheng, M.; Wang, W.; Xiong, W.; Yang, Y.; Qin, L.; Zhou, C.; Wang, H.; Zhou, Y.; Tian, S. Recent Progress on Metal-organic Frameworks Based- and Derived-Photocatalysts for Water Splitting. *Chem. Eng. J.* **2020**, *383*, 123196.

(4) Niu, F.; Wang, D.; Li, F.; Liu, Y.; Shen, S.; Meyer, T. J. Hybrid Photoelectrochemical Water Splitting Systems: From Interface Design to System Assembly. *Adv. Energy Mater.* **2019**, *10*, 1900399.

(5) Fujishima, A.; Honda, K. Electrochemical Photolysis of Water at a Semiconductor Electrode. *Nature* **1972**, *238*, 37.

(6) Miyoshi, A.; Nishioka, S.; Maeda, K. Water Splitting on Rutile TiO_2-Based Photocatalysts. *Chem. − Eur. J.* **2018**, *24*, 18204−18219.

(7) Matsubara, K.; Inoue, M.; Hagiwara, H.; Abe, T. Photocatalytic Water Splitting over Pt-loaded $TiO_2(Pt/TiO_2)$ Catalysts Prepared by the Polygonal Barrel-Sputtering Method. *Appl. Catal., B* **2019**, *254*, 7−14.

(8) Cheng, X.; Zhang, Y.; Hu, H.; Shang, M.; Bi, Y. High-efficiency $SrTiO_3/TiO_2$ Hetero-photoanode for Visible-light Water Splitting by Charge Transport Design and Optical Absorption Management. *Nanoscale* **2018**, *10*, 3644−3649.

(9) Chandrasekaran, S.; Kim, E. J.; Chung, J. S.; Yoo, I.-K.; Senthilkumar, V.; Kim, Y. S.; Bowen, C. R.; Adamaki, V.; Hur, S. H. Structurally Tuned Lead Magnesium Titanate Perovskite as a Photoelectrode Material for Enhanced Photoelectrochemical Water Splitting. *Chem. Eng. J.* **2017**, *309*, 682−690.

(10) Li, Z.; Yao, C.; Yu, Y.; Cai, Z.; Wang, X. Highly Efficient Capillary Photoelectrochemical Water Splitting Using Cellulose Nanofiber-Templated TiO_2 Photoanodes. *Adv. Mater.* **2014**, *26*, 2262−2267.

(11) Liu, N.; Schneider, C.; Freitag, D.; Hartmann, M.; Venkatesan, U.; Müller, J.; Spiecker, E.; Schmuki, P. *Nano Lett.* **2014**, *14*, 3309−3313.

(12) Pang, Y.; Zang, W.; Kou, Z.; Zhang, L.; Xu, G.; Lv, J.; Gao, X.; Pan, Z.; Wang, J.; Wu, Y. Assembling of Bi Atoms on TiO_2 Nanorods boosts Photoelectrochemical Water Splitting of Semiconductors. *Nanoscale* **2020**, *12*, 4302−4308.

(13) Fu, Y.; Dong, C.-L.; Zhou, W.; Lu, Y.-R.; Huang, Y.-C.; Liu, Y.; Guo, P.; Zhao, L.; Chou, W.-C.; Shen, S. A Ternary Nanostructured α-Fe_2O_3/Au/TiO_2 Photoanode with Reconstructed Interfaces for Efficient Photoelectrocatalytic Water Splitting. *Appl. Catal., B* **2020**, *260*, 118206.

(14) Sharma, P.; Jang, J.-W.; Lee, J. S. Key Strategies to Advance the Photoelectrochemical Water Splitting Performance of α-Fe_2O_3 Photoanode. *ChemCatChem* **2018**, *11*, 157−179.

(15) Chong, R.; Du, Y.; Chang, Z.; Jia, Y.; Qiao, Y.; Liu, S.; Liu, Y.; Zhou, Y.; Li, D. 2D Co-incorporated Hydroxyapatite Nanoarchitecture as a Potential Efficient Oxygen Evolution Cocatalyst for boosting Photoelectrochemical Water Splitting on Fe_2O_3 Photoanode. *Appl. Catal., B* **2019**, *250*, 224−233.

(16) Sivula, K.; Le Formal, F.; Grätzel, M. Solar Water Splitting: Progress Using Hematite (α-Fe_2O_3) Photoelectrodes. *ChemSusChem* **2011**, *4*, 432−449.

(17) Yu, Q.; Meng, X.; Wang, T.; Li, P.; Ye, J. Hematite Films Decorated with Nanostructured Ferric Oxyhydroxide as Photoanodes for Efficient and Stable Photoelectrochemical Water Splitting. *Adv. Funct. Mater.* **2015**, *25*, 2686−2692.

(18) Wang, L.; Lee, C.-Y.; Mazare, A.; Lee, K.; Müller, J.; Spiecker, E.; Schmuki, P. Enhancing the Water Splitting Efficiency of Sn-Doped Hematite Nanoflakes by Flame Annealing. *Chem. − Eur. J.* **2014**, *20*, 77−82.

(19) Han, H.; Kment, S.; Karlicky, F.; Wang, L.; Naldoni, A.; Schmuki, P.; Zboril, R. Sb-Doped SnO_2 Nanorods Underlayer Effect to the α-Fe_2O_3 Nanorods Sheathed with TiO_2 for Enhanced Photoelectrochemical Water Splitting. *Small* **2018**, *14*, 1703860.

(20) Xu, D.; Xia, T.; Xu, H.; Fan, W.; Shi, W. Synthesis of Ternary Spinel MCo_2O_4 (M = Mn, Zn)/$BiVO_4$ Photoelectrodes for Photolectrochemical Water Splitting. *Chem. Eng. J.* **2020**, *392*, 124838.

(21) Zhao, R.; Zhong, J.; Ji, C.; Zhao, J.; Lu, H. Three-dimensional $ZnO/Zn_xCd_{1-x}S/CdS$ Nanostructures Modified by Microwave Hydro-

thermal Reaction-deposited CdSe Quantum dots for Chemical Solar Cells. *Sol. Energy* **2019**, *191*, 78−83.

(22) Li, C.; Chen, Z.; Yuan, W.; Xu, Q.-H.; Li, C. M. In situ Growth of α-Fe_2O_3@Co_3O_4 Core-shell Wormlike Nanoarrays for a Highly Efficient Photoelectrochemical Water Oxidation Reaction. *Nanoscale* **2019**, *11*, 1111−1122.

(23) Yang, W.; Yu, Y.; Starr, M. B.; Yin, X.; Li, Z.; Kvit, A.; Wang, S.; Zhao, P.; Wang, X. Ferroelectric Polarization-Enhanced Photoelectrochemical Water Splitting in TiO_2-$BaTiO_3$ Core-Shell Nanowire Photoanodes. *Nano Lett.* **2015**, *15*, 7574−7580.

(24) Wang, X.; Li, Z.; Xu, W.; Kulkarni, S. A.; Batabyal, S. K.; Zhang, S.; Cao, A.; Wong, L. H. TiO_2 Nanotube Arrays Based Flexible Perovskite Solar Cells with Transparent Carbon Nanotube Electrode. *Nano Energy* **2015**, *11*, 728−735.

(25) Smith, W.; Wolcott, A.; Fitzmorris, R. C.; Zhang, J. Z.; Zhao, Y. Quasi-core-shell TiO_2/WO_3 and WO_3/TiO_2 Nanorod Arrays Fabricated by Glancing Angle Deposition for Solar Water Splitting. *J. Mater. Chem.* **2011**, *21*, 10792−10800.

(26) Zhao, R.; Chen, Y.; Ji, Y.; Li, W.; Chen, L.; He, A.; Lu, H.; Zhao, M.; Yao, J.; Jiang, Y.; Liu, G.; Gao, J.; Wang, H.; Yang, H. Controllable Conduction and Hidden Phase Transitions Revealed via Vertical Strain. *Appl. Phys. Lett.* **2019**, *114*, 252901.

(27) Milenov, T.; Dikovska, A.; Avdeev, G.; Avramova, I.; Kirilov, K.; Karashanova, D.; Terziyska, P.; Georgieva, B.; Arnaudov, B.; Kolev, S.; Valcheva, E. Pulsed Laser Deposition of Thin Carbon Films on SiO_2/Si Substrates. *Appl. Surf. Sci.* **2019**, *480*, 323−329.

(28) Wang, H.; Wu, Y.; Ma, M.; Dong, S.; Li, Q.; Du, J.; Zhang, H.; Xu, Q. Pulsed Laser Deposition of $CsPbBr_3$ Films for Application in Perovskite Solar Cells. *ACS Appl. Energy Mater.* **2019**, *2*, 2305.

(29) Ojeda-G-P, A.; Döbeli, M.; Lippert, T. Influence of Plume Properties on Thin Film Composition in Pulsed Laser Deposition. *Adv. Mater. Interfaces* **2018**, *5*, 1701062.

(30) Lu, H.; Zhong, J.; Ji, C.; Zhao, J.; Li, D.; Zhao, R.; Jiang, Y.; Fang, S.; Liang, T.; Li, H.; Li, C. M. Fabricating an Optimal Rutile TiO_2 Electron Transport Layer by Delicately Tuning $TiCl_4$ Precursor Solution for High Performance Perovskite Solar Cells. *Nano Energy* **2020**, *68*, 104336.

(31) Liu, Q.; Lu, H.; Shi, Z.; Wu, F.; Guo, J.; Deng, K.; Li, L. 2D $ZnIn_2S_4$ Nanosheet/lD TiO_2 Nanorod Heterostructure Arrays for Improved Photoelectrochemical Water Splitting. *ACS Appl. Mater. Interfaces* **2014**, *6*, 17200−17207.

(32) Prathan, A.; Sanglao, J.; Wang, T.; Bhoomanee, C.; Ruankham, P.; Gardchareon, A.; Wongratanaphisan, D. Controlled Structure and Growth Mechanism behind Hydrothermal Growth of TiO_2 Nanorods. *Sci. Rep.* **2020**, *10*, 8065.

(33) Soundarrajan, P.; Sankarasubramanian, K.; Sethuraman, K.; Ramamurthi, K. Controlled (110) and (101) crystallographic plane growth of single crystalline rutile TiO_2 nanorods by facile low cost chemical methods. *CrystEngComm* **2014**, *16*, 8756.

(34) Kalathil, S.; Khan, M. M.; Ansari, S. A.; Lee, J.; Cho, M. H. Band Gap Narrowing of Titanium Dioxide (TiO_2) Nanocrystals by Electrochemically Active Biofilms and Their Visible Light Activity. *Nanoscale* **2013**, *5*, 6323−6326.

(35) Kumar, P.; Rawat, N.; Hang, D.-R.; Lee, H.-N.; Kumar, R. Controlling Band Gap and Refractive Index in Dopant-Free α-Fe_2O_3 Films. *Mater. Lett.* **2015**, *11*, 13−23.